Microsystems and Nanosystems

Dan Zhang
Bin Wei *Editors*

Advanced Mechatronics and MEMS Devices II

Springer

Microsystems and Nanosystems

Series editors

Roger T. Howe, Stanford, CA, USA
Antonio J. Ricco, Moffett Field, CA, USA

More information about this series at http://www.springer.com/series/11483

Dan Zhang • Bin Wei
Editors

Advanced Mechatronics and MEMS Devices II

Springer

Editors
Dan Zhang
York University
Toronto, ON, Canada

Bin Wei
University of Ontario Institute of Technology
Oshawa, ON, Canada

ISSN 2198-0063 ISSN 2198-0071 (electronic)
Microsystems and Nanosystems
ISBN 978-3-319-32178-3 ISBN 978-3-319-32180-6 (eBook)
DOI 10.1007/978-3-319-32180-6

Library of Congress Control Number: 2012943040

© Springer International Publishing Switzerland 2017
This work is subject to copyright. All rights are reserved by the Publisher, whether the whole or part of the material is concerned, specifically the rights of translation, reprinting, reuse of illustrations, recitation, broadcasting, reproduction on microfilms or in any other physical way, and transmission or information storage and retrieval, electronic adaptation, computer software, or by similar or dissimilar methodology now known or hereafter developed.
The use of general descriptive names, registered names, trademarks, service marks, etc. in this publication does not imply, even in the absence of a specific statement, that such names are exempt from the relevant protective laws and regulations and therefore free for general use.
The publisher, the authors and the editors are safe to assume that the advice and information in this book are believed to be true and accurate at the date of publication. Neither the publisher nor the authors or the editors give a warranty, express or implied, with respect to the material contained herein or for any errors or omissions that may have been made.

Printed on acid-free paper

This Springer imprint is published by Springer Nature
The registered company is Springer International Publishing AG Switzerland

Preface

Mechatronics and robotics have been widely used in many arenas, such as manufacturing, medical, and space. With the rapid development of mechatronics and MEMS technologies, a follow-up edition of the book *Advanced Mechatronics and MEMS Devices* is deemed necessary. The aim of *Advanced Mechatronics and MEMS Devices II* is to introduce the state-of-the-art technologies in the field of mechatronics, robotics, and MEMS devices in order to further summarize and improve the methodologies of mechatronics and MEMS devices. Advances made in the past decades will be well described in this book, including mechatronics, robotics, and MEMS-related issues.

We would like to express our deep appreciation to all the authors for their significant contributions to the book. Their commitment, enthusiasm, and technical expertise are what made this book possible. We are also grateful to the publisher for supporting this project and would especially like to thank Marta Moldvai of Springer Science Business Media (USA) for her constructive assistance and cooperation, both with the publishing venture in general and the editorial details. We hope the readers find this book informative and useful.

This book consists of 30 chapters. Chapter 1 presents the theory and application of actuation of elastomeric micro-devices via capillary force technology. Chapter 2 provides insight into the fundamental design, working principles, and practical guidance of MEMS accelerometers. Details of experimental setups, signal conditioning, and data processing are also provided to construct an integrated performance assessment system. Chapter 3 gives an overview of the impact of the change from a focus on analysis, simulation, and modeling combined with outsourcing hardware design to the use of digital fabrication tools allowing a cyclic design process inside the lab, using many examples from various projects, and shares some insights and lessons learned for facilitating and implementing this process. Chapter 4 presents the design of a family of micro-robots capable of object manipulation in a fluidic environment. Chapter 5 discusses how state-of-the-art mobile technologies may be integrated into human-in-the-loop cyber-physical systems and exploited to provide natural mappings for remote interactions with such systems. A demonstrative example is used to show how an intuitive metaphor is

uncovered for performing a balancing task through the teleoperation of a ball and beam test bed. Chapter 6 provides an overview on force/tactile sensor development. By exploiting optoelectronic technology, two tactile sensors that can be used to execute both fine manipulation of objects and safe interaction tasks with humans are designed and realized. Chapter 7 addresses a brief account of issues related to mechanical properties of MEMS. Micro-testing techniques including micro-tensile and micro-fatigue testing along with the hardware are described with typical sample type, shape, and geometry, depicted with diagrams and images. Chapter 8 studies a type of marmot-like rescue robot for mine safety detection and rescuing. The kinematics, maximum stiffness, minimum stiffness, and global stiffness of the head section of the rescue robot are modeled and analyzed. Chapter 9 presents a systematic review of key control schemes for reconfigurable robotic systems, highlighting their benefits and disadvantages, and also reviews the application of these systems at microscale. Chapter 10 gives a detailed overview of MEMS-based sensors and actuators. Chapter 11 proposes a novel sensing approach to in situ particulate material (soot) load measurement in a diesel particulate filter using electrical capacitance tomography (ECT). Chapter 12 provides an overview of three actuation mechanisms that are relevant for biomedical applications of microfluidics. The topics dealt with include dielectrophoresis, acoustophoresis, and magnetophoresis. Chapter 13 reviews a few mechatronic devices designed and used in ASD screening and discusses a few devices used for therapeutic purposes. Chapter 14 conducts a critical and thorough review on vapor/gas sensing properties of a wide range of electrochemically derived metal oxide nano-forms as the sensing layer employing a different device configuration. Chapter 15 develops a wearable blood pressure monitoring system using ultrasound and a microperfusion system using a metal needle with micro-flow channel for measurement of subepidermal biological substances. Chapter 16 discusses the fabrication strategies and materials for the development of physical, chemical, and biosensors. The emerging applications of flexible electronics in wound healing, wearable electronics, implantable devices, and surgical tools, as well as point-of-care diagnostic devices, are also explored. Chapter 17 presents several MEMS devices where the main application is agriculture. Chapter 18 shows the design, fabrication, and testing of a multifunctional MEMS sensor for use in hydraulic systems. The MEMS device is incorporated into a typical fluid power component. Chapter 19 proposes a piezoelectric-actuated rigid nano-needle for single cell wall (SCW) cutting. A fabricated tungsten (W) nano-needle is assembled with a commercial piezoelectric actuator laterally and perpendicularly. Chapter 20 develops a process planning-driven approach for the development of a robotic percussive riveting system for aircraft assembly automation. Chapter 21 introduces photoinduced fabrication technologies for 3D MEMS devices and examines four technologies and their outcome of applications where fabricated feature sizes decrease and resolution increases. Chapter 22 presents a design principle of the OKES by deriving a mathematical model and characterized the OKES performance in terms of working range, positioning accuracy, resolution, linearity, bandwidth, and control effectiveness with the nano-positioning systems. Chapter 23 presents a lab-on-chip microfluidics system for SCM measurement,

related to the force required to drag a single cell and Newton's law of motion inside microfluidics channel. Chapter 24 focuses on the characteristics of micro-manipulation in terms of the types and principles of gripping forces. Chapter 25 discusses three important aspects of inertial microfluidics: fundamental mechanism, microchannel designs, and applications. Chapter 26 provides a detailed overview of the different types of piezoelectric force sensors and the dynamic calibration techniques that have been used to calibrate these sensors. Chapter 27 introduces a magnetically driven micro-robotics system to explain the procedure of developing a magnetic levitation stage and proposes a sensor switching mechanism that combines magnetic flux measurement-based position determination and optical sensor-based position detection. Chapter 28 applies 3D printing molding methods to fabricate a miniature magnetic actuator for an optical image stabilizer, and the application of robust control techniques to actuate the developed miniature magnetic actuators is discussed. Chapter 29 deals with the concept of biofeedback control systems and its structure, and various applicable control methods which are designed to fulfill different system requirements are provided. Chapter 30 develops an inverse adaptive controller design method for the purpose of mitigating the hysteresis effect in the magnetostrictive-actuated dynamic systems.

Finally, we would like to sincerely acknowledge all the friends and colleagues who have contributed to this book.

Toronto, ON, Canada Dan Zhang
Oshawa, ON, Canada Bin Wei
February 2016

Contents

1 Actuation of Elastomeric Micro Devices via Capillary Forces 1
Carl R. Knospe and Christina Barth

2 MEMS Accelerometers: Testing and Practical Approach for Smart Sensing and Machinery Diagnostics 19
A. Albarbar and S.H. Teay

3 Highlights in Mechatronic Design Approaches 41
Edwin Dertien and Stefano Stramigioli

4 Microrobots for Active Object Manipulation 61
Roel S. Pieters, Hsi-Wen Tung, and Bradley J. Nelson

5 Integrating Smart Mobile Devices for Immersive Interaction and Control of Physical Systems: A Cyber-Physical Approach 73
Jared A. Frank and Vikram Kapila

6 Force/Tactile Sensors Based on Optoelectronic Technology for Manipulation and Physical Human–Robot Interaction 95
Andrea Cirillo, Pasquale Cirillo, Giuseppe De Maria, Ciro Natale, and Salvatore Pirozzi

7 Mechanical Characterization of MEMS 133
Seyed M. Allameh

8 Basic Theory and Modelling of Marmot-Like Robot for Mine Safety Detection and Rescuing 153
Dan Zhang and Bin Wei

9 Reconfigurable Robot Manipulators: Adaptation, Control, and MEMS Applications 169
Gokhan Gungor, Baris Fidan, and William W. Melek

10 MEMS Sensors and Actuators 195
Vishwas N. Bedekar and Khalid Hasan Tantawi

11 Soot Load Sensing in a Diesel Particulate Filter Based on Electrical Capacitance Tomography 217
Ragibul Huq and Sohel Anwar

12 Microfluidic Platforms for Bio-applications 253
Anas Alazzam, Bobby Mathew, and Saud Khashan

13 Recent Advances in Mechatronics Devices: Screening and Rehabilitation Devices for Autism Spectrum Disorder 283
Hadi Moradi and Iman Mohammad-Rezazadeh

14 Electrochemically Derived Oxide Nanoform-Based Gas Sensor Devices: Challenges and Prospects with MEMS Integration 297
P. Bhattacharyya, K. Dutta, and P.P. Chattopadhyay

15 Minimally Invasive Medical Devices and Healthcare Devices Using Microfabrication Technology 329
Y. Haga, T. Matsunaga, T. Kobayashi, and N. Tsuruoka

16 Flexible Electronic Devices for Biomedical Applications 341
Pooria Mostafalu, Amir Sanati Nezhad, Mehdi Nikkhah, and Mohsen Akbari

17 MEMS Devices in Agriculture 367
Antonio Valente

18 MEMS Pressure-Flow-Temperature Sensor for Hydraulic Systems .. 387
Charles Groepper, Perry Y. Li, Tianhong Cui, and Kim A. Stelson

19 Vibrating Nanoneedle for Single Cell Wall Cutting 421
Md. Habibur Rahman, Abdul Hafiz Mat Sulaiman, Mohd Ridzuan Ahmad, Masahiro Nakajima, and Toshio Fukuda

20 A Robotic Percussive Riveting System for Aircraft Assembly Automation 443
Fengfeng (Jeff) Xi, Yu Lin, and Yuwen Li

21 Photo-Induced Fabrication Technology for 3D Microdevices 469
D. Serien, Y. Morimoto, and S. Takeuchi

22 Long-Range Nano-Scanning Devices Based on Optical Sensing Technology 495
ChaBum Lee

23 Microfluidics for Mass Measurement of Miniature Object Like Single Cell and Single MicroParticle 523
Md. Habibur Rahman, Mohd Ridzuan Ahmad, Masaru Takeuchi, Masahiro Nakajima, Yasuhisa Hasegawa, and Toshio Fukuda

24 Micromanipulation Tools 547
Jin Li and Zhuming Bi

25 Inertial Microfluidics: Mechanisms and Applications 563
Jun Zhang, Weihua Li, and Gursel Alici

26 Force Sensing for Micro/Meso Milling 595
Yu Hui Feng and Goldie Nejat

27 Magnetically Driven Microrobotics for Micromanipulation and Biomedical Applications 613
Xiaodong Zhang and Mir Behrad Khamesee

28 Design, Fabrication, and Robust Control of Miniaturized Optical Image Stabilizers 637
Kaiwen Yuan, Alireza Alizadegan, Pan Zhao, Ryozo Nagamune, Jingsong Chu, Simon Park, and Mu Chiao

29 Biofeedback Technologies for Wireless Body Area Networks 659
Rui Li, Daniel T.H. Lai, and Wee Sit Lee

30 Inverse Adaptive Controller Design for Magnetostrictive-Actuated Dynamic Systems 687
Zhi Li, Chun-Yi Su, and Xiuyu Zhang

Index 715

Contributors

Mohd Ridzuan Ahmad Department of Control and Mechatronics Engineering, Faculty of Electrical Engineering, Universiti Teknologi Malaysia, Johor, Malaysia

Mohsen Akbari Department of Mechanical Engineering, Laboratory for Innovation in MicroEngineering (LiME), University of Victoria, Victoria, BC, Canada

Center for Biomedical Research, University of Victoria, Victoria, BC, Canada

Anas Alazzam Department of Mechanical Engineering, Khalifa University, Abu Dhabi, UAE

A. Albarbar School of Engineering, Manchester Metropolitan University, Manchester, UK

Gursel Alici School of Mechanical, Materials and Mechatronic Engineering, University of Wollongong, Wollongong, NSW, Australia

ARC Center of Excellence for Electromaterials Science, University of Wollongong, Wollongong, NSW, Australia

Alireza Alizadegan Department of Mechanical Engineering, University of British Columbia, Vancouver, BC, Canada

Seyed M. Allameh Northern Kentucky University, Highland Heights, KY, USA

Sohel Anwar Department of Mechanical Engineering, Purdue School of Engineering and Technology, Indiana Univ Purdue Univ Indianapolis, Indianapolis, IN, USA

Christina Barth Department of Mechanical and Aerospace Engineering, University of Virginia, Charlottesville, VA, USA

Vishwas N. Bedekar Department of Engineering Technology, Middle Tennessee State University, Murfreesboro, TN, USA

P. Bhattacharyya Department of Electronics and Telecommunication Engineering, Indian Institute of Engineering Science and Technology, Shibpur, Howrah, West Bengal, India

Zhuming Bi Department of Civil and Mechanical Engineering, Indiana University Purdue University Fort Wayne, Fort Wayne, IN, USA

P.P. Chattopadhyay Department of Metallurgy and Materials Engineering, Indian Institute of Engineering Science and Technology, Shibpur, Howrah, West Bengal, India

Mu Chiao Department of Mechanical Engineering, University of British Columbia, Vancouver, BC, Canada

Jingsong Chu Micromolding Solutions Inc., Brossard, QC, Canada

Andrea Cirillo Dipartimento di Ingegneria Industriale e dell'Informazione, Seconda Università degli Studi di Napoli, Aversa, Italy

Pasquale Cirillo Dipartimento di Ingegneria Industriale e dell'Informazione, Seconda Università degli Studi di Napoli, Aversa, Italy

Tianhong Cui University of Minnesota, Minneapolis, MN, USA

Edwin Dertien Robotics and Mechatronics Group, Faculty of Electrical Engineering, Mathematics and Computer Science, University of Twente, Enschede, The Netherlands

K. Dutta Department of Electronics and Telecommunication Engineering, Indian Institute of Engineering Science and Technology, Shibpur, Howrah, West Bengal, India

Giuseppe De Maria Dipartimento di Ingegneria Industriale e dell'Informazione, Seconda Università degli Studi di Napoli, Aversa, Italy

Yu Hui Feng Autonomous Systems and Biomechatronics Laboratory, Department of Mechanical and Industrial Engineering, University of Toronto, Toronto, ON, Canada

Baris Fidan University of Waterloo, Waterloo, ON, Canada

Jared A. Frank NYU Tandon School of Engineering, Brooklyn, NY, USA

Toshio Fukuda Institute for Advanced Research, Nagoya University, Nagoya, Aichi, Japan

Faculty of Science and Engineering, Meijo University, Nagoya, Aichi, Japan

Intelligent Robotics Institute, School of Mechatronic Engineering, Beijing Institute of Technology, Beijing, China

Charles Groepper AT Instruments, Cardiff, UK

University of Minnesota, Minneapolis, MN, USA

Gokhan Gungor University of Waterloo, Waterloo, ON, Canada

Y. Haga Graduate School of Biomedical Engineering, Tohoku University, Sendai, Japan

Ragibul Huq Cummins, Inc., Columbus, IN, USA

Vikram Kapila NYU Tandon School of Engineering, Brooklyn, NY, USA

Mir Behrad Khamesee University of Waterloo, Waterloo, ON, Canada

Saud Khashan Department of Mechanical Engineering, Jordan University of Science and Technology, Irbid, Jordan

Jordan University of Science and Technology, Irbid, Jordan

Carl R. Knospe Department of Mechanical and Aerospace Engineering, University of Virginia, Charlottesville, VA, USA

T. Kobayashi Graduate School of Biomedical Engineering, Tohoku University, Sendai, Japan

Daniel T.H. Lai College of Engineering and Science, Victoria University, Footscray, VIC, Australia

ChaBum Lee Department of Mechanical Engineering, Tennessee Technological University, Cookeville, TN, USA

Wee Sit Lee College of Engineering and Science, Victoria University, Footscray, VIC, Australia

Jin Li Complex and Intelligent System Research Laboratory (CISRL), School of Mechanical and Power Engineering, East China University of Science and Technology, Shanghai, China

Perry Y. Li University of Minnesota, Minneapolis, MN, USA

Rui Li College of Engineering and Science, Victoria University, Footscray, VIC, Australia

Weihua Li School of Mechanical, Materials and Mechatronic Engineering, University of Wollongong, Wollongong, NSW, Australia

Yuwen Li School of Mechatronic Engineering and Automation, Shanghai University, Shanghai, China

Zhi Li Eindhoven University of Technology, Eindhoven, MB, The Netherlands

Yu Lin Kirchhoff Van-Rob, Aurora, ON, Canada

Bobby Mathew Department of Mechanical Engineering, Khalifa University, Abu Dhabi, UAE

T. Matsunaga Micro System Integration Center, Tohoku University, Sendai, Japan

William W. Melek University of Waterloo, Waterloo, ON, Canada

Iman Mohammad-Rezazadeh Semel Institute for Neuroscience and Human Behavior, UCLA David Geffen School of Medicine, Los Angeles, CA, USA

Hadi Moradi School of Electrical and Computer Engineering, University of Tehran, Tehran, Iran

Intelligent Systems Research Institute, SKKU, Suwon, South Korea

Y. Morimoto Institute of Industrial Science, The University of Tokyo, Tokyo, Japan

Takeuchi Biohybrid Innovation Project, Exploratory Research for Advanced Technology, Japan Science and Technology, Tokyo, Japan

Pooria Mostafalu Harvard-MIT Division of Health Sciences and Technology, Massachusetts Institute of Technology, Cambridge, MA, USA

Wyss Institute for Biologically Inspired Engineering, Harvard University, Boston, MA, USA

Ryozo Nagamune Department of Mechanical Engineering, University of British Columbia, Vancouver, BC, Canada

Ciro Natale Dipartimento di Ingegneria Industriale e dell'Informazione, Seconda Università degli Studi di Napoli, Aversa, Italy

Goldie Nejat Autonomous Systems and Biomechatronics Laboratory, Department of Mechanical and Industrial Engineering, University of Toronto, Toronto, ON, Canada

Bradley J. Nelson Institute of Robotics and Intelligent Systems, ETH Zurich, Zurich, Switzerland

Amir Sanati Nezhad Department of Mechanical and Manufacturing Engineering, BioMEMS and Bioinspired Microfluidic Laboratory, Schulich School of Engineering, University of Calgary, Calgary, AB, Canada

Mehdi Nikkhah School of Biological and Health Systems Engineering, Arizona State University, Tempe, AZ, USA

Simon Park Schulich School of Engineering, University of Calgary, Calgary, AB, Canada

Roel S. Pieters Institute of Robotics and Intelligent Systems, ETH Zurich, Zurich, Switzerland

Salvatore Pirozzi Dipartimento di Ingegneria Industriale e dell'Informazione, Seconda Università degli Studi di Napoli, Aversa, Italy

D. Serien Institute of Industrial Science, The University of Tokyo, Tokyo, Japan

Takeuchi Biohybrid Innovation Project, Exploratory Research for Advanced Technology, Japan Science and Technology, Tokyo, Japan

Kim A. Stelson University of Minnesota, Minneapolis, MN, USA

Stefano Stramigioli Robotics and Mechatronics Group, Faculty of Electrical Engineering, Mathematics and Computer Science, University of Twente, Enschede, The Netherlands

Chun-Yi Su Concordia University, Montreal, QC, Canada

S. Takeuchi Institute of Industrial Science, The University of Tokyo, Tokyo, Japan

Takeuchi Biohybrid Innovation Project, Exploratory Research for Advanced Technology, Japan Science and Technology, Tokyo, Japan

Khalid Hasan Tantawi Department of Career Readiness-Mechatronics, Motlow State Community College, Smyrna, TN, USA

S.H. Teay School of Engineering, Manchester Metropolitan University, Manchester, UK

N. Tsuruoka Graduate School of Biomedical Engineering, Tohoku University, Sendai, Japan

Antonio Valente INESC TEC (formerly INESC Porto) and School of Science and Technology, UTAD University, Vila Real, Portugal

Bin Wei Faculty of Engineering and Applied Science, University of Ontario Institute of Technology, Oshawa, ON, Canada

Fengfeng (Jeff) Xi Department of Aerospace Engineering, Ryerson University, Toronto, ON, Canada

Kaiwen Yuan Department of Mechanical Engineering, University of British Columbia, Vancouver, BC, Canada

Dan Zhang Department of Mechanical Engineering, York University, Toronto, ON, Canada

Jun Zhang School of Mechanical, Materials and Mechatronic Engineering, University of Wollongong, Wollongong, NSW, Australia

Xiuyu Zhang Northeast Dianli University, Jilin, China

Xiaodong Zhang University of Waterloo, Waterloo, ON, Canada

Pan Zhao Department of Mechanical Engineering, University of British Columbia, Vancouver, BC, Canada

Chapter 1
Actuation of Elastomeric Micro Devices via Capillary Forces

Carl R. Knospe and Christina Barth

Abstract Elastomeric materials offer many benefits to MEMS, including smaller device footprints, greater range of motion, and lower required actuation forces. Capillary forces are a novel and promising mechanism to produce motion in the flexible components of microdevices that contain them. Through the phenomenon of electrowetting these forces can be actively controlled, offering a unique capability to achieve large motions with small voltages. The theory and application of this technology is reviewed herein. Experimental results are also presented illustrating the significant potential of the approach for a wide array of applications.

Keywords Capillary force • Electrowetting • Actuator • Microfluidics • MEMS • Dielectric • Microdevice • Elastomeric • Electrolyte • Large stroke • Low voltage • Adaptive optics • Lab-on-a-chip

1 Introduction

1.1 Hybrid Microdevices

The advantages of hybrid microdevices with soft elastomeric components are increasingly being recognized [1–3]. Elastomeric components have a much lower modulus of elasticity than the silicon typically employed in MEMS. As a result, elastomeric flexures do not require the large footprint demanded by micromachined silicon flexures to achieve low compliance. Lower modulus also means that hybrid devices require less actuation force to realize a desired deflection. This reduces both the on-chip space needed for actuators and the actuation power. Elastomeric materials also permit much higher strain (>100 %) than silicon, allowing significantly greater linear and rotational motion of components. Additionally, elastomeric

C.R. Knospe (✉) • C. Barth
Department of Mechanical and Aerospace Engineering, University of Virginia, Charlottesville, VA, USA
e-mail: knospe@virginia.edu

© Springer International Publishing Switzerland 2017

D. Zhang, B. Wei (eds.), *Advanced Mechatronics and MEMS Devices II*,
Microsystems and Nanosystems, DOI 10.1007/978-3-319-32180-6_1

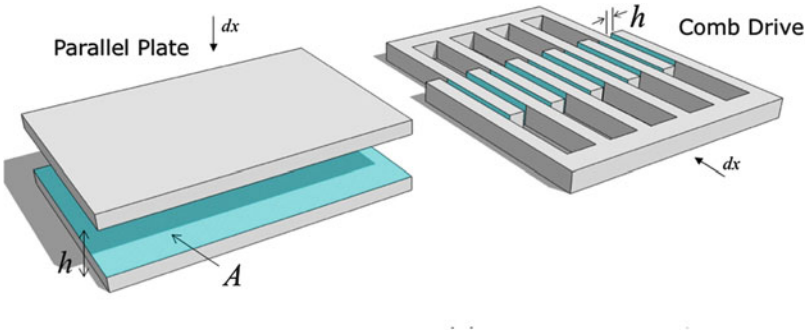

Fig. 1.1 Parallel plate and comb drive electrostatic actuators

materials enable a tight, yet reversible, seal to be formed between surfaces. Thus, on-chip valves and pumps for microfluidic applications can be more easily realized.

A suitable actuation technology is needed, however, to complement the capabilities of elastomeric components, one that full advantage of the high compliance, large deformations, and structural reconfigurability of soft components. While a variety of MEMS actuating technologies are available, including electrostatic, electromagnetic, piezoelectric, and thermal, existing technologies are not up to the task. Each approach has significant disadvantages with respect to one or more of the following performance metrics: force capability, actuator stroke, power required, bandwidth, and ease of integration with elastomeric components [4–7].

To illustrate, let us consider electrostatic actuators, the most commonly used MEMS technology. These can be classified into parallel plate and comb configurations—see Fig. 1.1. In the former, motion is normal to the electrode surfaces and in the later it is parallel with them. As a result, stroke is directly limited by electrode gap in the former. In general, actuators in this family are simple to fabricate using photolithographic micromachining since they do not require materials or elements that are difficult to integrate into microfabrication. Electrostatic actuators typically require voltages much higher than is desirable for MEMS, often greater than 60 V. In many applications, these actuators are very large in comparison to the actuation stroke due to several factors including: (1) limited actuation stroke necessitates significant mechanical amplification to achieve the required range of motion; (2) limitations on device voltage result in large electrode surfaces to achieve the force production required for the application, and for comb drive in particular; (3) the achievable accuracy of lithographically defined features results in relatively large electrostatic gaps, decreasing actuator effectiveness; and (4) "side snap-over" instability limits achievable force and stroke.

In this chapter the electrically controlled capillary forces are investigated for the actuation of elastomeric components in hybrid MEMS. As will be shown, capillary force actuation can achieve significantly greater forces than can be obtained by similarly sized electrostatic actuators. Furthermore, results demonstrate that large actuation strokes can be realized without mechanical amplification.

1.2 Capillary Forces

Consider a liquid droplet in contact with a solid surface and surrounded by a medium, either gas or liquid, referred to as the *ambient*. The contact line surrounding the wetted area of the solid surface has a radius r_c. The interface between the droplet and the ambient has a surface energy, referred to simply as the droplet's surface tension and denoted σ_{al}. The surface energy of the interface between the solid surface and, respectively, the liquid and the ambient will be denoted as σ_{ls} and σ_{as}. The contact angle of the liquid with the solid surface, θ, is determined by these surface energies via $\cos\theta = (\sigma_{as} - \sigma_{ls})/\sigma_{al}$.

Two types of forces are exerted on the solid surface by the droplet: (1) surface tension forces acting at the three phase contact line and tangential to the free interface and (2) Laplace pressure forces acting over the wetted area and normal to the solid's surface [8] (Fig. 1.2). The static pressure difference between the ambient and the liquid is given by Laplace's equation:

$$p = \sigma_{al}\left(\frac{1}{R_1} + \frac{1}{R_2}\right) \tag{1.1}$$

where R_1 and R_2 are the radii of curvature of the liquid's free interface. To illustrate the difference between the surface tension and Laplace forces acting upon a surface consider the case of a short liquid bridge extending between two parallel solid planar surfaces as shown in Fig. 1.3. The radii of curvature at the bridge's waist are $R_1 = r_1$

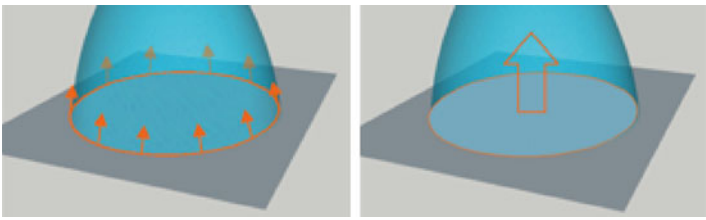

Fig. 1.2 Two types of forces exerted by a liquid droplet upon a solid surface—*Left*: surface tension force acting at the contact line, $F_\sigma = 2\pi r_c \sigma_{al} \sin\theta$; *Right*: Laplace pressure acting over wetted area, $F_p = \pi r_c^2 p$

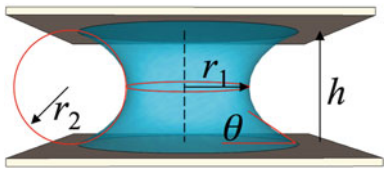

Fig. 1.3 Geometry of axisymmetric liquid bridge extending between two parallel surfaces of spacing h illustrating radii of curvature of interface

and $R_2 = -r_2 = -h\cos(\theta/2)$. The surface tension force, F_σ, is then found by a line integral of the surface tension over the contact line:

$$F_\sigma = -2\pi\sigma_{\mathrm{al}}\sin\theta \tag{1.2}$$

where the negative sign indicates that this force is acting to bring the solid surfaces closer together. The Laplace pressure is

$$p = \sigma_{\mathrm{al}}\left(\frac{1}{r_1} - \frac{2\cos\theta}{h}\right) \tag{1.3}$$

The integral of the pressure over the wetted area ($r_1 \sim r_{\mathrm{c}}$) yields the force due to the Laplace pressure:

$$F_p = \pi r_{\mathrm{c}}^2 p = \pi r_{\mathrm{c}}\sigma_{\mathrm{al}}\left\{1 - 2\left(\frac{r_{\mathrm{c}}}{h}\right)\cos\theta\right\} \tag{1.4}$$

The net force exerted upon the solid surface by the drop is then

$$F = \pi r_{\mathrm{c}}\sigma_{\mathrm{al}}\left\{1 - 2\sin\theta - 2\left(\frac{r_{\mathrm{c}}}{h}\right)\cos\theta\right\} \tag{1.5}$$

The Laplace pressure force will be much larger than the surface tension force if $h \ll r_{\mathrm{c}}$ [8]. Since the Laplace pressure is inversely dependent on the radii of curvature, as the magnitude of the radius R_2 is decreased the magnitude of the Laplace pressure increases rapidly. If properly engineered, capillary forces can provide a highly effective means for actuation in hybrid MEMS.

To illustrate the potential of capillary forces for the deformation of elastomeric microdevices, consider the novel transpiration actuator described by Borno et al. [3] and shown in Fig. 1.4. This passive polymeric microdevice, inspired by the spore dispersal mechanism of ferns, uses the capillary forces of water between ribs to deform the elastic spine connecting the ribs. When not loaded with water, the spine has a circular form of diameter ≈ 1 mm. When water is added, the spine straightens and extends due to the capillary forces acting upon the ribs. As the water evaporates, the spine returns to its original circular form. Between the wetted and dry state the spine's tip moves more than 3.5 mm and rotates more than 330°.

The scaling of capillary forces is particularly well suited for the deformation of such soft structures, inspiring many innovative concepts such as the recently developed capillary origami [9] shown in Fig. 1.5.

Micromechanical systems employing capillary forces do not need to be passive devices like those above. Capillary forces can also be electrically controlled via the phenomenon of electrowetting on dielectric (EWOD). In electrowetting the application of an electrical potential to a conducting liquid placed on a dielectric-covered electrode causes the liquid to spread upon the dielectric surface [10–14]. The apparent contact angle of the liquid on the surface decreases and the surface acts

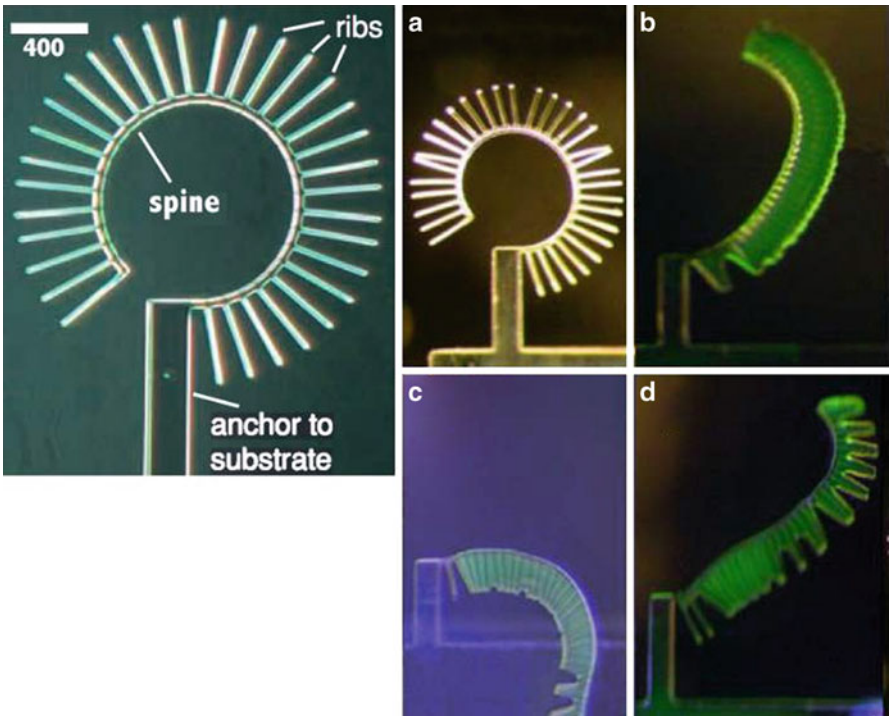

Fig. 1.4 Uncoiling elater—*Left*: microdevice geometry and scale (400 m). *Right*: (**a**) dry device before filling water between fins; (**b**) 0.5 s after filling, device has begun initial deformation due to capillary pressure acting to pull fins together; (**c**) full deflection, 2 s after filling; (**d**) 20 s after filling, evaporation has begun to return the device to its original state. Figure adapted from Borno et al. [3], doi:10.1088/0960-1317/16/11/018 © IOP Publishing. Reproduced with permission. All rights reserved

as increasingly hydrophilic. This change in contact angle results in a change in the curvature of the droplet's free interface and thus induces a change in droplet internal pressure. This change in pressure is the key to capillary force actuation, a novel and promising approach to actuation in MEMS [15–18]. The promise of electrically activated capillary forces for actuation was demonstrated for a conventional MEMS device in [18]. In the experiment a liquid bridge was placed between a fixed plate electrode and a plate electrode supported by micromachined beam flexures. Both electrodes were manufactured from silicon wafers that were covered by a 30 nm oxide film and a 30 nm hydrophobic polymer. The liquid bridge was 100 μm in height and approximately 1 mm in diameter. A maximum deflection of 5 μm was achieved with 40 V applied. This corresponds to an actuation force of over 200 μN. For comparison, a parallel plate electrostatic actuator with the same area and electrode gap would achieve only 3 μN at this voltage. Thus, forces greater than *60 times that of* electrostatic actuation can be achieved via capillary pressure.

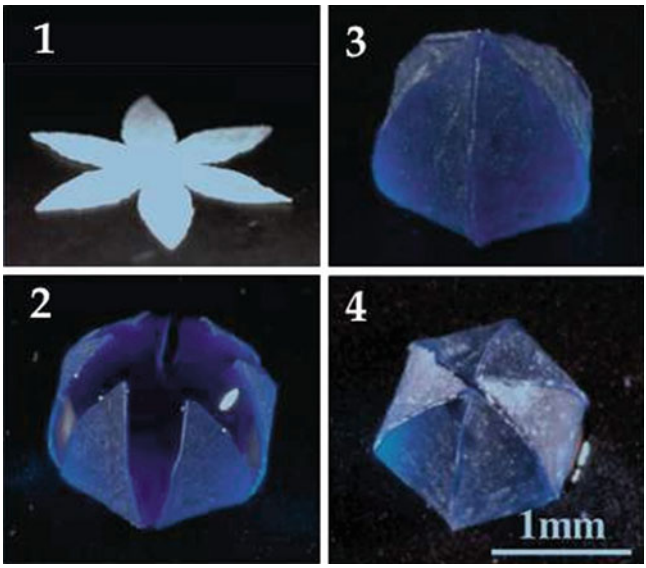

Fig. 1.5 Capillary origami–an elastic planar sheet wraps around a droplet to encapsulate it. (1) sheet before droplet's addition; (2) during the process of encapsulation; (3-4) final configuration. Reprinted figure with permission from [9]. Copyright 2007 by the American Physical Society

In the following section the characteristics of electrowetting that are particularly relevant to the actuation of hybrid microdevices are reviewed.

2 Electrowetting

2.1 Introduction

Consider a typical electrowetting experimental setup (Fig. 1.6): a sessile droplet is surrounded by an ambient gas. The dielectric layer is an oxide that is covered by a thin fluoropolymer topcoat to render the surface hydrophobic and to minimize contact angle hysteresis so as to allow easy movement of the contact line upon the surface. The droplet is an aqueous solution of an inorganic salt. An electric potential is applied between a wire inserted into the drop and the electrode.

Ideally, the change in apparent contact angle in electrowetting is governed by the Young-Lippmann equation:

$$\cos\theta_v = \cos\theta_0 + \frac{\varepsilon_\mathrm{d}}{2\sigma_\mathrm{al} t_\mathrm{d}} v_\mathrm{d}^2 \tag{1.6}$$

where θ_v is the apparent contact angle of the liquid with applied field, θ_0 is the native contact angle (without field), ε_d is the permittivity of the dielectric, t_d is the thickness

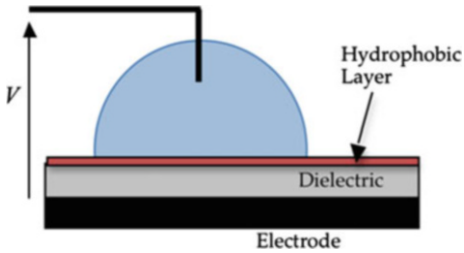

Fig. 1.6 Typical electrowetting on dielectric (EWOD) setup

of the dielectric layer, and v_d is the voltage across the layer. Equation (1.6) predicts that perfect wetting (i.e., zero contact angle) will be achieved at a finite voltage. In practice, however, the contact angle will cease to decrease beyond a certain voltage, a phenomenon known as *contact angle saturation*. A variety of mechanisms have been proposed for contact angle saturation, most of which are related to the leakage of charge near the contact line. These include instability of the contact line and expulsion of satellite droplets; charge trapping in the dielectric layer; and electrical breakdown of the dielectric layer [10, 11, 13]. More than one of these mechanisms may contribute to anomalous electrowetting behavior at higher voltages.

2.2 Physics of Electrowetting

Electrowetting is an electromechanical phenomenon in which the applied electric field causes an electrostatic pressure on the liquid surface near the contact line [10]. Thus, it is important to understand the interactions of electric field, ions, and liquid to understand the dynamics of capillary force actuation and how to engineer devices to achieve performance metrics. This discussion will begin with the case of a perfectly conducting liquid. As the liquids typically employed have very high conductivities, this assumption is a reasonable one to begin; its shortcomings will be examined afterwards. When electric potential is applied, it causes an electric field, which results in the migration of ions in the liquid. In the perfectly conducting case, the free charge appears at liquid's interface and screens the electric field from the liquid's interior. An electrostatic pressure is applied to the interface by the interaction of the ions with the electric field induced by the applied voltage [14]. In response to this pressure the conducting liquid is pulled outward causing increased wetting of the substrate. The electrostatic pressure also strongly affects the curvature of the liquid/ambient interface proximate to the contact line. Since the surface energy of the solid/liquid interface is unchanged, the actual contact angle in electrowetting is not altered by the application of voltage—it remains θ_0. The effective contact angle that determines the free interface, however, does change with applied potential and it is typically measured via optical imaging. It is this change in apparent contact angle that is captured by the Young-Lippmann equation, Eq. (1.6). The transition of the liquid profile tangent from native contact angle (θ_0) to apparent contact angle (θ_v) is not easily imaged since the characteristic length scale of the transition is the dielectric thickness. With significant electrowetting the

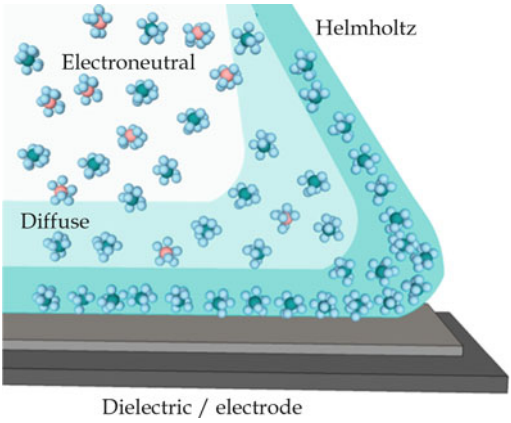

Fig. 1.7 Helmholtz/diffuse layer model of solvated ions near the contact line during electrowetting (size of ions greatly exaggerated for purposes of illustration)

pressure associated with the high concentration of ionic charge and field in this region results in strong local curvature of the gas–liquid interface. The local electric field present in the dielectric layer is dependent on both the electric potential of the liquid and the shape of the interface in this region. In short, application of electric potential results in charge migration, the alteration of the liquid profile, and the redistribution and concentration of the local electric field in the dielectric layer. Thus, the transition region plays a critical role in the mechanisms of charge leakage and electrical breakdown that are thought to result in contact angle saturation and decreased electrowetting performance. In the more realistic case of liquids that do not act as perfect conductors, the transition layer's structure will depend upon the influences of thermal, electrical, and intermolecular forces. Standard models of the liquid/ambient interface consist of a surface layer of oriented water molecules (since dipoles tend to align with field), followed by a Helmholtz lamina of solvated ions, and then a diffuse region of ions in which the potential falls exponentially to that of the bulk (electroneutrality) [19], see Fig. 1.7. We would expect the combined thickness of the Helmholtz and diffuse regions to be in the range of 1–10 nm, depending on ions, solvent, and field. It is clear that these dimensions are not negligible in comparison to the characteristic length scale of the transition region (10–100 nm).

3 Capillary Actuation Dynamics

In examining the actuation dynamics it is useful to consider the time constants of various phenomena in the chain of events that ensue after a change in applied voltage. In a previous paper [16] the author explored this in detail for conventional MEMS devices with capillary actuation via electrowetting. Many of the insights obtained also hold for elastomeric devices and are therefore useful for the present discussion.

When a step in voltage is applied to a hybrid capillary device, there will first be a charging of the dielectric's capacitance. This would occur very quickly with a time constant of about 0.1 μs. Then, the contact angle would change; flow would occur only proximate to the free interface. The time constant for this behavior would be on the order of 10 μs. The local change in interface shape would then set up a pressure differential causing further changes to the free interface, bulk droplet flow, and the beginning of movement/deformation of any participating adjacent elastomeric surfaces. With bulk flow, the liquids free interface would continue to advance and change shape, but at each time instant it would approximately assume an energy-minimizing surface (due to the small time constant associated with capillary waves)—i.e., quasi-static behavior. Typically, the period of bulk flow and solid surface movement would be on the order of 10 ms, slowly ending in the device reaching a new equilibrium and flow ceasing at about 100 ms.

These dynamics are governed by nonlinear differential equations with the nonlinearities arising from four sources: (1) the change in wetted area with the motion of elastomeric surfaces arising from volume conservation; (2) the nonlinear damping introduced by the squeezing of liquid between surfaces; (3) the Lippmann-Young electrowetting equation, and (4) nonlinear elastic behavior associated with large displacements of flexible components. The first source is responsible for any "snap down" (saddle node) bifurcation if it occurs in a hybrid device.

4 Advantages

Capillary force actuation has several advantages for hybrid microdevices.

Large Stroke. Like electrostatic comb drive actuators, capillary force devices produce force through increasing the stored capacitive energy with deflection by increasing the capacitive area. Therefore, the gap between electrodes can remain constant during deflection, unlike the case of electrostatic parallel plate actuators. This feature decouples the thickness of the energy storing capacitance from the actuation stroke. Thus, the thickness can be made as small as practical (so as to improve force capability) without requiring any sacrifice of actuator stroke.

Large Pressure Changes. The pressure change that can be achieved depends on several factors including saturation contact angle, geometry of the free interface, and surface tension of the liquid. The last of these would not be important if contact angle saturation did not occur as it would otherwise cancel out in the governing equations. In all cases, the key factor is the change in capacitance with deformation of the flexible element. The thickness associated with the capacitive energy storage should be as thin as practical so as to maximize this change. With electrowetting actuation this thickness can be much smaller than is achievable with comb drive actuation, 50 nm in comparison to 1000 nm. Furthermore, the permittivity of the capacitive element may be three to ten times greater than the gap in comb drive. Thus, pressures 60 times greater than electrostatic actuation can be achieved, as has been demonstrated in experiments [18].

Application of Pressure to All Surfaces in Contact with Droplet. One key feature of this approach that makes it particularly well suited to the actuation of elastomeric components is that the pressure acts upon all surfaces in contact with the liquid, not just those that contain electrodes, unlike electrostatic actuation. Thus, capillary pressure can be used to deform soft structural elements that do not contain electrodes. This capability can enhance the types of deformations that can be induced and greatly simplify device fabrication. Since the liquid conforms with flexible components as they change shape the pressure will continue to act even after dramatic changes in shape. This capability is made clear by example of capillary origami [9] (Fig. 1.5).

5 Applications

Flexible capillary microdevices have many potential applications ranging from medical care to astronomical optics. Here several potential applications are examined.

Lab-on-a-Chip. Over the past decade rapid progress has been made in the miniaturization of chemical and biological analysis onto microdevices, often referred to as Lab-on-a-Chip [20]. This technology holds many promises including smaller samples, quicker analysis, and parallel processing capability. Critical to this technology is the ability to manage the flow of nanoliter samples in a network of microchannels through flow control devices such as valves and pumps. Active valves technologies today suffer from slow response speed, large power requirements, and bulky off-chip equipment. For example, one common design employs an elastomeric membrane as the valve moving-element, with actuation of this membrane accomplished pneumatically using an external air pump. Similar designs are common for flow generation, including peristaltic and diaphragm pumps [21]. To reduce device size, minimize power consumption, and enhance portability, development of a totally integrated microfluidic device, with flow control integrated on the substrate, is highly desirable. Capillary pressure is an ideal mechanism for the deformation of membranes (or other soft structures) in microfluidic devices, as the electrodes do not need to be integrated into the soft elements.

Adaptive Optics. Adaptive optics systems correct image distortion through the adjustment of the surface shape of a deformable mirror (DM) to alter the light wavefront. AO systems are now common in astronomical imaging and are making inroads into diagnostic retinal imaging [22–26]. Mirror shape change is achieved by electrical signals to arrays of actuators behind the mirror surface. Today, most adaptive optics systems use an array of piezoelectric or electrostatic actuators to deform the DM surface. Actuation requires high voltages and only a limited range of motion (about 1 μm) can be achieved. NSF's Roadmap for the Development of Astronomical Adaptive Optics found that actuation technology for adaptive optics was a "significant technical hurdle" for future telescopes. The report cited large stroke (up to 10 μm) deformable mirrors as a "high priority investment need" [23]. For clinical ophthalmic applications, DMs also need greater stroke for retinal imaging (up to 50 μm) so as to adjust for wavefront errors that occur in the eyes of

the patient population [26]. The required accuracy and stability of motion control for adaptive optics applications is a small fraction of a wavelength and therefore feedback control is typically used in these systems.

Braille Displays. Over 40 million people worldwide are blind and have great difficulty using computers, tablets, e-readers, and cell phones, in spite of the advent of text-to-speech software. Current refreshable Braille displays are both prohibitively expensive and too bulky for these applications [27]. Their complexity also precludes the display of a full page of text, requiring the reader to alter her reading patterns. To achieve a refreshable Braille display with low cost, weight, and power, will require a large stroke actuation technology (300–500 μm) that can be manufactured by high throughput processes such as photolithography and inkjet printing. The required force for holding a raised dot during reading is 0.15 N [27]. However, if actuation is used to release and lower the dot, then it is not necessary that this force level is achieved by the microactuator.

Microendoscopes. Recently miniaturized laser-scanning microendoscopes have been developed for clinical use and biomedical research [28, 29]. These devices require large stroke actuation for x-y scanning and focal depth adjustment. Such devices, if equipped with a significant frame rate, could perform minimally invasive diagnostics in the lungs, urinary tract, and ovaries; and guide therapeutic interventions. This technology could have a profound impact upon health care, eliminating the need for unnecessary, costly, and worrisome biopsies for many patients. Typically, these systems require strokes of 100 μm or more and a scan frequency greater than 10 Hz [29].

6 Example

To illustrate the use of energy approaches for analysis of hybrid devices with capillary actuation an example problem will be examined here. This analysis also illustrates the interplay of surface tension, elastic bending forces, and electrostatic forces in the static behavior of hybrid devices.

Consider the hybrid device illustrated in Fig. 1.8. An elastomeric rectangular membrane of length l and width w is in contact with a droplet that electrowets into a hydrophobic cavity of height h width w. The membrane without any applied forces has curvatures 0 about the x axis and $1/R_u$ about the y axis. The droplet wets the entire underside of the membrane and is pinned along one edge of the membrane and one edge of the cavity structure. The top surface of the cavity is an electrode and the bottom surface is an electrode covered with a dielectric thickness t_d, and permittivity ε_d. The net surface tensions of the top ($i = 1$) and bottom ($i = 2$) surfaces are given by $\sigma_i = \sigma_{\mathrm{ls}_i} - \sigma_{\mathrm{as}_i}$ where σ_{ls_i} and σ_{as_i} are the surface energies of the liquid/solid and ambient/solid interfaces. The contact angles of the liquid on these two surfaces (without applied voltage) are denoted $\theta_{(1)}$ and $\theta_{(2)}$. The angle of the membrane tangent at its end is denoted ψ. For this analysis the complex liquid interface shape at the device ends (extremes of y) will be approximated by planes as we seek an analytic result; if the width is sufficiently large this approximation will have little impact as the energy associated with end effects will be small. It is assumed that as

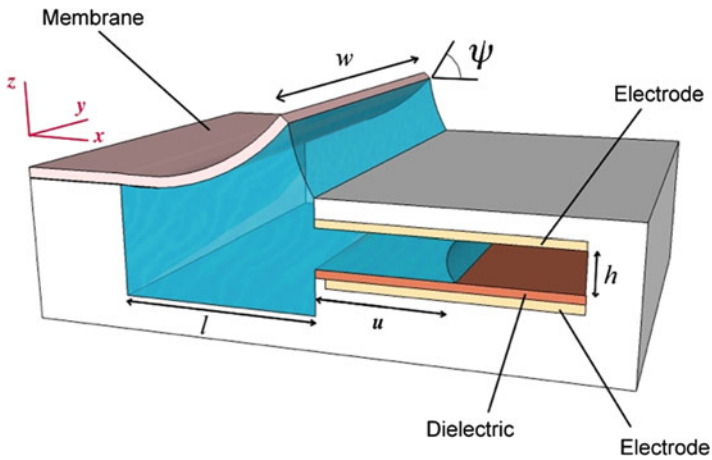

Fig. 1.8 Capillary force actuation of elastomeric membrane in hybrid MEMS device

electrowetting into the cavity occurs the membrane will continue to have uniform curvature with that about the x axis remaining 0. This along with the assumption about end effects yields a single degree of freedom problem. Finally, it is assumed that the variation in area of the liquid/ambient interface within the cavity is small as electrowetting occurs; this is reasonable if the cavity height h is small in comparison to other dimensions. Denote the penetration of the liquid into the cavity by u.

Since the membrane has constant curvature throughout and the length l is constant, the radius of curvature R and the membrane tangent angle ψ are related by

$$R = \frac{l}{\psi} \tag{1.7}$$

From trigonometry, the total volume of liquid is given by

$$\mathcal{V} = \frac{w}{2}\left(\frac{l}{\psi}\right)^2 (\sin\psi - \psi\cos\psi) + uwh + \mathcal{V}_{\text{dead}} \tag{1.8}$$

where the last term is the dead volume in the device. Taylor series expansion of the first term and linear approximation yields:

$$\mathcal{V} = \frac{wl^2}{6}\psi + uwh + \mathcal{V}_{\text{dead}} \tag{1.9}$$

This expression is well justified for $0 \leq \psi < 0.9$ rad. Since volume is conserved this expression upon differentiation yields:

$$\frac{du}{d\psi} = -\frac{l^2}{6h} \tag{1.10}$$

The total liquid/ambient surface area can be found via trigonometry and approximated (again, after Talyor series expansion) as:

$$\mathcal{S}_{\mathrm{al}} = \left(\frac{wl}{2} + \frac{l^2}{3}\right)\psi + wh \tag{1.11}$$

The total energy of the device is the sum of the capacitive energy, ambient/liquid interface energy, liquid/solid interface energy, and membrane bending energy:

$$E_{\mathrm{total}} = E_{\mathrm{cap}} + E_{\mathrm{al}} + E_{\mathrm{ls}} + E_{\mathrm{bend}} \tag{1.12}$$

The first of these is based on the capacitance of the wetted area of the dielectric:

$$E_{\mathrm{cap}} = -\left(\frac{1}{2}\right)\frac{\varepsilon_{\mathrm{d}} wu}{t_{\mathrm{d}}}\, v_{\mathrm{d}}^2 \tag{1.13}$$

and the second and third terms are simply the surface tension multiplied by the interface area:

$$E_{\mathrm{al}} = \sigma_{\mathrm{al}}\mathcal{S}_{\mathrm{al}} E_{\mathrm{ls}} = (\sigma_1 + \sigma_2)\, wu \tag{1.14}$$

The bending energy can be found in terms of the mean curvature of the membrane with applied capillary pressure (H) and without (H_u)

$$E_{\mathrm{bend}} = \frac{1}{2}K_b(H - H_u)^2 wl \tag{1.15}$$

where K_b is the flexural rigidity, H is the membrane mean curvature, given by

$$H = \frac{1}{2}\left(\kappa_x + \kappa_y\right) \tag{1.16}$$

and the membrane curvatures are $\kappa_x = 0$ and $\kappa_y = 1/R$. For the membrane without applied capillary pressure these quantities are $\kappa_x = 0$ and $\kappa_y = 1/R_u$. Hence, the bending energy is:

$$E_{\mathrm{bend}} = \frac{1}{2}K_b\left(\frac{1}{2R} - \frac{1}{2R_u}\right)^2 wl \tag{1.17}$$

Using Eq. (1.7) this relation can be expressed in terms of the membrane tip tangent angle as:

$$E_{\mathrm{bend}} = \frac{1}{8}K_b\frac{w}{l}(\psi - \psi_u)^2 \tag{1.18}$$

The minimum of the total energy with respect to ψ is the equilibrium for a given voltage. Setting the differential of E_{total} with respect to ψ equal to zero yields the desired expression after some algebra:

$$\psi = \psi_u + 4\frac{l^2}{K_b}\left\{\frac{l}{6h}(\sigma_1 + \sigma_2) - \left(\frac{1}{2} + \frac{l}{3w}\right)\sigma_{\text{al}}\right\} - \frac{1}{3}\left(\frac{l^2}{K_b}\right)\left(\frac{l}{h}\right)\left(\frac{\varepsilon_{\text{d}}}{t_{\text{d}}}\right)v_{\text{d}}^2 \tag{1.19}$$

The membrane tip tangent angle with no voltage applied, $\psi_0\psi_0$, therefore is:

$$\psi_0 = \psi_u + 4\frac{l^2}{K_b}\left\{\frac{l}{6h}(\sigma_1 + \sigma_2) - \left(\frac{1}{2} + \frac{l}{3w}\right)\sigma_{\text{al}}\right\} \tag{1.20}$$

Thus, the no voltage angle ψ_0 is greater than the angle present with no capillary force acting, ψ_0, (i.e., device not loaded with liquid) if

$$\sigma_1 + \sigma_2 > \left(\frac{3h}{l} + \frac{2h}{w}\right)\sigma_{\text{al}} \tag{1.21}$$

Since $\sigma_1/\sigma_{\text{al}} = -\cos\theta_{(i)}$ this condition is:

$$-\cos\theta_{(1)} - \cos\theta_{(2)} > \left(\frac{3h}{l} + \frac{2h}{w}\right) \tag{1.22}$$

which will occur only if the upper and lower surfaces of the cavity are sufficiently hydrophobic. Otherwise, when the droplet is loaded into the structure the capillary pressure will pull the membrane down. Using the contact angle relations Eq. (1.20) can be rewritten as:

$$\psi_0 = \psi_u - \frac{2\sigma_{\text{al}}l^3}{3K_b h}\left\{\cos\theta_{(1)} + \cos\theta_{(2)} + \left(\frac{3h}{l} + \frac{2h}{w}\right)\right\} \tag{1.23}$$

From Eq. (1.19), the membrane tangent angle as a function of voltage is therefore:

$$\psi = \psi_0 - \frac{1}{3}\left(\frac{l^2}{K_b}\right)\left(\frac{l}{h}\right)\left(\frac{\varepsilon_{\text{d}}}{t_{\text{d}}}\right)v_{\text{d}}^2 \tag{1.24}$$

Hence, the degree of membrane actuation at a given voltage is improved by (1) increasing the dielectric permittivity ε_{d} and decreasing dielectric thickness t_{d}; (2) increasing the ratio of membrane length l to cavity height h, and (3) decreasing the membrane flexural rigidity K_b.

Consider a device with a PDMS membrane with an 80 μm thickness, 500 μm length, 180 μm width, and membrane tip angle of 40° (without liquid). Suppose that the cavity has height of 40 μm and that the liquid has a contact angle on the upper and lower surfaces of 110°. Furthermore, let the dielectric thickness be 70 nm

and its relative permittivity be 3. After the liquid has been placed in contact with the membrane the membrane tip angle will remain unchanged. As voltage is applied to the device the membrane will uncurl until it achieves a flat configuration ($\psi = 0$) when 10 V is applied.

7 Experimental Results

To illustrate the potential of electrically controlled capillary forces for the actuation of soft structures, consider the actuated membrane prototype developed by the authors (Fig. 1.9). This device has achieved a large actuation stroke while operating with low voltage. The device is composed of a conducting liquid droplet extending between two parallel plates. The upper plate consists of a glass slide in which a 875 μm hole has been laser cut. A 40 μm thick PDMS layer was placed on the top surface of the glass, covering the hole, to form the membrane. The bottom surface of the upper plate was coated with a gold layer to form an electrode. The lower plate

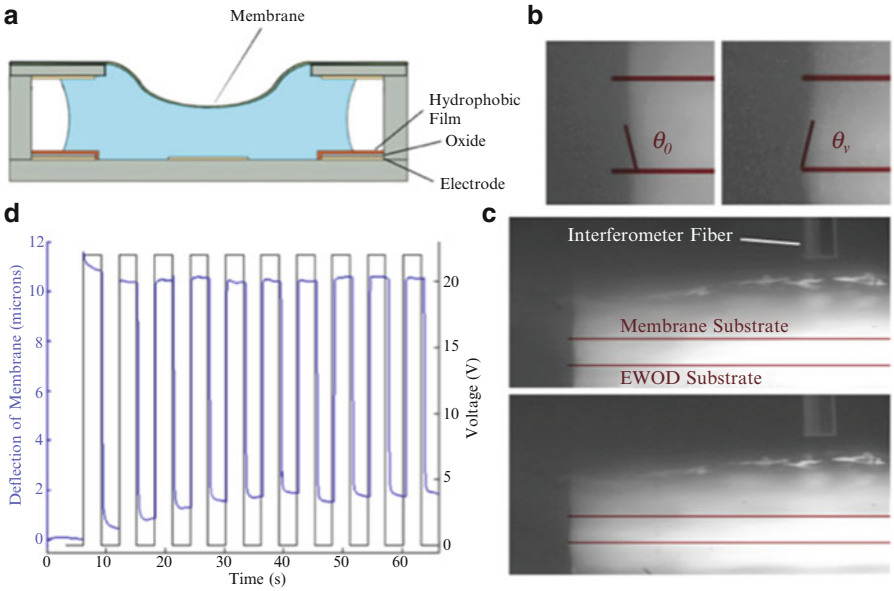

Fig. 1.9 Actuation of an elastomeric membrane via an electrowetting-induced change in capillary pressure. (**a**) Illustration of device configuration; (**b**) close-up images showing change in contact angle on the EWOD substrate, left image is 0 V, right image is 22 V. Droplet is bright due to fluorescence. Location of upper and lower electrodes indicated by *lines*, spacing is 120 mm; (**c**) entire images for 0 and 22 V showing optical fiber used for interferometric measurement of membrane deflection. Multiple droplet images appear due to reflection; and (**d**) membrane deflection and applied voltage during cycling test